JOURNAL OF SPACECRAFT AND ROCKETS
Vol. 42, No. 4, July–August 2005

Trajectory and Attitude Simulation for Aerocapture and Aerobraking

Mrinal Kumar* and Ashish Tewari†
Indian Institute of Technology, Kanpur 208 016, India

A combined strategy of aerocapture and aerobraking is presented to achieve a near-circular orbit, starting from a hyperbolic trajectory, without requiring an orbital insertion burn. Aerothermodynamic force, moment, and heat flux calculations employ a Maxwellian free-molecular flow model, with Knudsen-number-based interpolations for the transition regime. The six-degree-of-freedom motion model, including quaternion-based attitude dynamics, allows stability and sensitivity analyses for the atmospheric passes. A spacecraft model with two large panels suitable for Earth aerocapture is considered. Minor orbit-correction burns at the apoapsis are provided after each pass for manipulating the periapsis for the next pass to meet the desired aerobraking corridor. It is observed that an initial orbit of eccentricity 1.6 and relative entry velocity of 12 km/s at 300-km altitude can be reduced to an orbit with an eccentricity of 0.02, using a total of six atmospheric passes, without exceeding the peak convective heat flux constraint for the spacecraft or requiring an orbit insertion burn. This result has considerable importance for low-Earth-orbit space-tug captures and Mars missions, wherein the strategy proposed will lead to significant savings in spacecraft propellant mass during the orbit insertion and, subsequently, orbit circularization.

Nomenclature

A	=	reference area
a_c	=	thermal accommodation coefficient
C_p	=	pressure coefficient
C_τ	=	tangential stress coefficient
c	=	reference length
d_∞	=	freestream dynamic pressure
e	=	orbital eccentricity
$\boldsymbol{F}$	=	external force vector, $\in\Re^{3\times 1}$
$\boldsymbol{J}$	=	inertia tensor of the spacecraft, $\in\Re^{3\times 3}$
J_{11}, J_{22}, J_{33}	=	principal moments of inertia of the spacecraft
Kn	=	Knudsen number
$\boldsymbol{M}$	=	external moment vector, $\in\Re^{3\times 1}$
m	=	mass of the spacecraft
$\hat{\boldsymbol{n}}_i$	=	unit normal vector of the ith surface panel
p, q, r	=	angular velocity components about the X, Y, and Z body axes
Q	=	convective heat load on the spacecraft
$\dot{Q}$	=	convective heat flux
$\dot{Q}_{\max}$	=	maximum convective heat flux
q_0, q_1, q_2, q_3	=	quaternion components used to describe body orientation
R	=	distance of spacecraft center of mass from the planet's center
$\boldsymbol{r}_i$	=	position vector of the ith panel centroid relative to the center of mass of the spacecraft, $\boldsymbol{r}_i \in \Re^{3\times 1}$
$\boldsymbol{S}(\boldsymbol{\omega})$	=	skew-symmetric matrix, $\in\Re^{3\times 3}$
s	=	molecular speed ratio
T_W/T_∞	=	ratio of wall temperature to freestream temperature
V	=	spacecraft velocity measured in the planet fixed coordinate system
$X_{\text{fo}}, Y_{\text{fo}}, Z_{\text{fo}}$	=	forces along the wind axes
α	=	angle of attack
β_∞	=	parameter analogous to an inverse continuum speed of sound, $s = V\beta_\infty$
γ	=	flight-path angle, defined as the inclination of the velocity vector with respect to the instantaneous local horizon, positive above the horizon
$\tilde{\gamma}$	=	specific heat ratio of air, 1.4
δ	=	longitude, positive toward east
Θ	=	inclination of an elemental panel with respect to flow direction
θ_1, θ_2	=	deployment angles of the left and right panels of the spacecraft
λ	=	latitude, positive above the equator
ρ_∞	=	freestream density
σ_N	=	normal momentum accommodation coefficient
σ_T	=	tangential momentum accommodation coefficient
ς	=	angle of sideslip
χ	=	heading angle, defined as the azimuth of the velocity vector's projection on the local horizontal plane, positive toward north
Ω	=	rotational rate of the planet
$\boldsymbol{\omega}$	=	angular velocity vector of the spacecraft, $\in\Re^{3\times 1}$

Superscripts

$*$	=	inertial frame
$\cdot$	=	time derivative

Introduction

MODERN spacecraft mission design has grown in sophistication with every passing year. Several novel techniques have been incorporated into mission profiles and have proved beneficial to the overall mission structure. Aerobraking[1–4] is one such revolutionary technique, which was executed for the first time by the Magellan spacecraft[5] in 1992, although not as a part of the planned mission. Aerobraking is a method of reducing the spacecraft velocity by making it pass through the higher reaches of a planetary atmosphere, thereby using the concomitant drag as an "aerodynamic brake." The reduction in speed leads to a reduction in the orbit size when the spacecraft emerges from the atmosphere after the pass. Aerobraking had to wait until 1997 to become an integral part of a mission, when the Mars Global Surveyor (MGS) achieved a near-circular orbit, starting from the highly eccentric orbit resulting from

Received 17 December 2003; revision received 8 May 2004; accepted for publication 1 June 2004.

*Undergraduate Student, Department of Aerospace Engineering.
†Associate Professor, Department of Aerospace Engineering; ashtew@iitk.ac.in. Senior Member AIAA.

the Mars orbit insertion (MOI), by executing the repetitive maneuver spanning over 850 passes.[6–8] Both the Magellan and the MGS missions proved the basic technology of aerobraking, which was later applied to the Mars Odyssey[8] and the Mars Reconnaissance Orbiter mission designs.

In the available literature, reentry trajectory optimization generally ignores the attitude dynamics of the spacecraft.[9–13] Such studies employ constant aerodynamic parameters (drag and lift coefficients). These assumptions can be considered restrictive to the generality of the problem, because there can be appreciable changes in the body attitude during reentry. However, three-degree-of-freedom (DOF) studies are generally considered sufficient for trajectory design and analysis, in which the entry corridor is predetermined by a separate group of engineers studying aerothermal loads and specified as design constraints. As an exception, Johnson et al.[14] discussed attitude control during the reentry maneuver in their study, thereby incorporating the rigid-body motion of the spacecraft while maintaining simplified forms of the equations and using constant aerodynamic parameters.

After Magellan, the focus shifted to the Aeroassisted Flight Experiment, which drew the attention of researchers to the problem of an aeroassisted transfer of a spacecraft from a high earth orbit to a low Earth orbit (LEO).[9] However, with the cancellation of the experiment in 1995, the concentration of research could not go beyond the concept of aerobraking, which first needed to be proved. This was done by the MGS in 1997 and by the Odyssey in 2001. Therefore, now, the next logical step toward mission optimization is the aerocapture maneuver. Aerocapture is defined as an atmospheric pass employed to reduce a hyperbolic orbit to a bound, elliptic one. A complete study of the aerocapture maneuver, consisting of a trajectory analysis with attitude dynamics and aerothermal constraints, has not been reported. The most critical design requirement for an aerocapture mission is the rate of heat transfer (heat flux) because of atmospheric entry at a hyperbolic velocity. Due to the heat flux limitations, the guidance during aerocapture must necessarily be more precise than that for an elliptical reentry, and many researchers have focused on appropriate guidance strategies. Puig-Suari et al.[15] considered the aerocapture of a tethered satellite, whereas Powell and Braun[13] presented guidance laws during a Mars aerocapture maneuver, without discussing the expected heat flux magnitudes. French and Cruz[3] estimated that peak convective heat transfer rates of the order of 500 W/cm^2 could be expected during aerocapture, whereas Lohar et al.[16] gave higher estimates of the heat flux of a spacecraft executing an aerogravity assist maneuver, in which the velocities are similar to that for an Earth return mission. Selecting materials that can withstand the large heat flux expected in aerocapture is a major design problem. Among new ablative materials, the phenolic-impregnated carbon ablator[17] (PICA) is capable of handling extreme heat transfer rates up to 1500 W/cm^2. PICA has been used on the Stardust Comet Return Capsule,[18] which will reenter Earth at a relative velocity of 12.6 km/s in the year 2006.

The present study aims to solve a generalized problem of the atmospheric pass. The dynamic model incorporates all six DOF of a rigid spacecraft, hence enabling the stability and sensitivity analysis during the pass. Although a precise attitude control strategy in the exoatmospheric phase is always adopted to produce a desirable reentry attitude, it is possible that such control may be anomalous. Therefore, in an anomalous attitude and spin rate at reentry, it is necessary to see whether the spacecraft can be stabilized in the atmospheric phase without a functioning attitude control. We confine ourselves in this study to open-loop simulations of trajectory and attitude parameters and their sensitivity to geometric configurations and off-design initial conditions. The simulations for the atmospheric passes are initiated at a geometric altitude of 300 km with a 21-layer, standard atmosphere to accurately determine the entry corridor for aerocapture. Despite the tenuous atmosphere at such altitudes, a hyperbolic entry, coupled with the fact that the drag coefficient is the highest in the free-molecular regime, may lead to considerable drag force. Furthermore, to carefully study the rotational stability and sensitivity with respect to large initial angles of attack and sideslip, caused by a possible failure of an onboard attitude control system, the initial conditions must be specified at a high altitude. In comparison, most previous studies have considered entry altitudes in the range 120–150 km.

After a bound orbit is established by the aerocapture (Fig. 1), it is transformed into a circular orbit by executing further passes in a series of approximate Hohmann ellipses. The number of passes required will depend on the available heat-shielding capacity of the thermal protection system of the spacecraft.[3] In this paper, the peak convective heat flux for the first pass has been kept at 450 W/cm^2. Minor orbit-correction burns at the apoapsis are required after each pass for manipulating the periapsis for the next pass to keep the spacecraft in the desired corridor for aerobraking.[5] The stability analysis of the maneuvers shows that active control would be not be required while inside the atmosphere.

The aerodynamic model used first identifies the flow over the spacecraft as either free-molecular, transition, or continuum, depending on the Knudsen number of the freestream. The force and moment coefficients are calculated at each time step of integration by a local surface inclination panel method employing Maxwellian

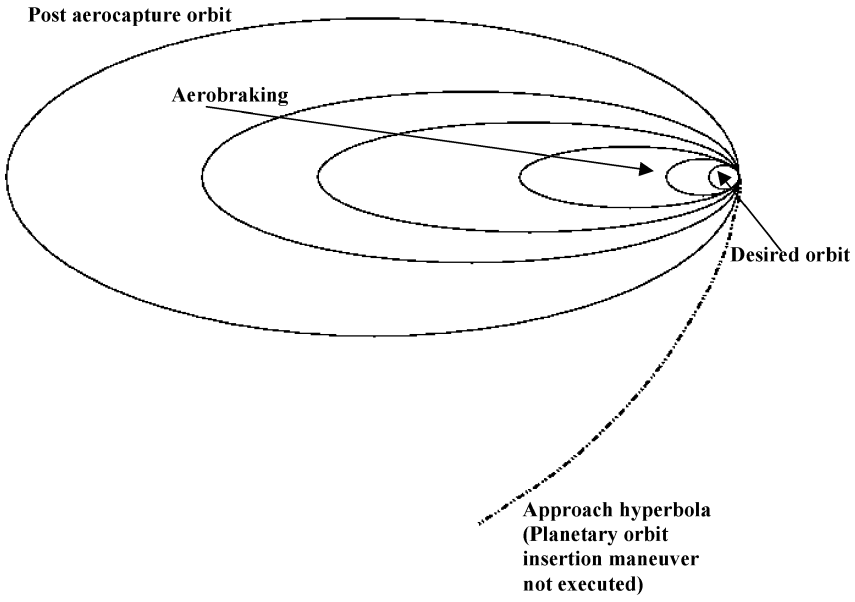

Fig. 1 Schematic of orbit reduction caused by aerobraking.

velocity distribution of reflected particles. The results of this study may be applied to a planetary return to LEO (such as a space tug) or extended to a Mars mission, which will mean a significant saving of spacecraft propellant mass, given proper shielding for the spacecraft.

Dynamic Model

The planet-centered, nonrotating frame is taken as the inertial reference coordinate system. The equations of motion[12,19] for the atmospheric phase are standard and have been developed in a planet-centric frame, rotating with the planet. Quaternion-based formulation is undertaken to preclude the possibility of singularities at a pitch angle of 90 deg, which is otherwise a problem with the Euler-angle formulation. The aerodynamic model calculates forces and moments with respect to the body axes. They are transformed to the wind axes via the inertial axes before being employed in the equations of motion given as follows.

The kinematic equations of particle motion are the following[12,19]:

$$\dot{\delta} = \frac{V \cos\gamma \cos\chi}{R \cos\lambda} \tag{1}$$

$$\dot{\lambda} = \frac{V \cos\gamma \sin\chi}{R} \tag{2}$$

$$\dot{R} = V \sin\gamma \tag{3}$$

The kinetic equations of particle motion (inside the atmosphere) can be written as follows[12,19]:

$$\dot{V} = -g \sin\gamma + \frac{Y_{\text{fo}}}{m} + \Omega^2 R \cos\lambda(\sin\gamma \cos\lambda - \cos\gamma \sin\chi \sin\lambda) \tag{4}$$

$$\dot{\gamma} = \left(\frac{V}{R} - \frac{g}{V}\right)\cos\gamma + \frac{X_{\text{fo}}}{Vm} + 2\Omega \cos\chi \cos\lambda + \frac{\Omega^2 R \cos\lambda(\cos\gamma \cos\lambda + \sin\gamma \sin\chi \sin\lambda)}{V} \tag{5}$$

$$\dot{\chi} = \frac{-V \cos\gamma \cos\chi \tan\lambda}{R} + \frac{Z_{\text{fo}}}{mV \cos\gamma} + 2\Omega(\tan\gamma \sin\chi \cos\lambda - \sin\lambda) - \frac{\Omega^2 r \cos\chi \cos\lambda \sin\lambda}{V \cos\gamma} \tag{6}$$

After emerging from the atmosphere, the spacecraft swings around in the resulting elliptical orbit before reentering the atmosphere. This exoatmospheric phase has been solved with the Keplerian equations of particle motion written in the inertial frame. These may be obtained in the same manner as the preceding equations, with the state variables being all inertial quantities:

$$\dot{\delta}^* = \frac{V^* \cos\gamma^* \cos\chi^*}{R^* \cos\lambda^*} \tag{7}$$

$$\dot{\lambda}^* = \frac{V^* \cos\gamma^* \sin\chi^*}{R^*} \tag{8}$$

$$\dot{R}^* = V^* \sin\gamma^* \tag{9}$$

$$\dot{V}^* = -g \sin\gamma^* + \frac{Y^*_{\text{fo}}}{m} \tag{10}$$

$$\dot{\gamma}^* = \left(\frac{V^*}{R^*} - \frac{g}{V^*}\right)\cos\gamma^* \tag{11}$$

$$\dot{\chi}^* = \frac{-V^* \cos\gamma^* \cos\chi^* \tan\lambda^*}{R^*} \tag{12}$$

In Eq. (10), the thrust Y^*_{fo} is nonzero only at the apoapsis, where an impulsive burn is applied to manipulate the periapsis for the next atmospheric pass. The following relationships relate the inertial variables with the noninertial variables[9]:

$$\delta^* = \delta + \Omega t \tag{13}$$

$$\lambda^* = \lambda \tag{14}$$

$$R^* = R \tag{15}$$

$$V^* \sin\gamma^* = V \sin\gamma \tag{16}$$

$$V^* \cos\gamma^* \sin\chi^* = V \cos\gamma \sin\chi \tag{17}$$

$$V^* \cos\gamma^* \cos\chi^* = V \cos\gamma \cos\chi + \Omega R \cos\lambda \tag{18}$$

The kinematic equations of rotational motion are as follows[20]:

$$\dot{q}_0 = -0.5(q_1 p + q_2 q + q_3 r) \tag{19}$$

$$\dot{q}_1 = 0.5(q_0 p + q_2 r - q_3 q) \tag{20}$$

$$\dot{q}_2 = 0.5(q_0 q + q_3 p - q_1 r) \tag{21}$$

$$\dot{q}_3 = 0.5(q_0 r + q_1 q - q_2 p) \tag{22}$$

$$q_0^2 + q_1^2 + q_2^2 + q_3^2 = 1 \tag{23}$$

The kinetic equations of rotational motion are the following[20]:

$$\dot{\boldsymbol{\omega}} = \boldsymbol{J}^{-1}(\boldsymbol{M} - \boldsymbol{S}(\boldsymbol{\omega})\boldsymbol{J}\boldsymbol{\omega}), \qquad \boldsymbol{\omega} = \{p, q, r\}^T$$

$$\boldsymbol{S}(\boldsymbol{\omega}) = \begin{bmatrix} 0 & -r & q \\ r & 0 & -p \\ -q & p & 0 \end{bmatrix} \tag{24}$$

Aerothermodynamic Model

The aerothermodynamic model is based on a Maxwellian velocity distribution of the reflected particles. The spacecraft profile is developed using three- or four-sided elemental flat panels. As long as the body is convex with respect to the freestream, the assumption of collisionless nature of the reflected particles is valid. The flowfield is classified on the basis of Knudsen number as follows[20]: $Kn \geq 10$ (free-molecular flow), $0.01 \leq Kn < 10$ (transition flow), and $Kn < 0.01$ (continuum flow).

For the free-molecular regime, the forces and moments are calculated on the assumption of diffuse reflection of particles from the body surface. For most engineering surfaces interacting with air, a_c, σ_N, and σ_T are all experimentally observed to be close to unity.[20] The thermal accommodation coefficient a_c is defined as a ratio of energy fluxes, depicting the particle–surface interaction as follows[20,21]:

$$a_c = \frac{\mathrm{d}E_i - \mathrm{d}E_r}{\mathrm{d}E_i - \mathrm{d}E_W} \tag{25}$$

where $\mathrm{d}E_W$ is the energy flux, were the distribution of the reflected particles given by the Maxwellian distribution. Similarly, σ_N and σ_T are defined as[20]

$$\sigma_N = (p_i - p_r)/(p_i - p_W), \qquad \sigma_T = (\tau_i - \tau_r)/\tau_i \tag{26}$$

Assuming $a_c = \sigma_N = \sigma_T = 1$, the following relations describe the pressure, shear stress, and convective heat flux on an elemental panel[20]:

$$\frac{\Delta p}{d_\infty} s^2 = \left(\frac{2 - \sigma_N}{\sqrt{\pi}} s \sin\Theta + \frac{\sigma_N}{2}\sqrt{\frac{T_W}{T_\infty}}\right) e^{-s^2 \sin^2\Theta} + \left[(2 - \sigma_N)(0.5 + s^2 \sin^2\Theta) + \frac{\sigma_N}{2}\sqrt{\frac{T_W}{T_\infty}}\pi s \sin\Theta\right] \times [1 + \operatorname{erf}(s \sin\Theta)] \tag{27}$$

$$\frac{\Delta\tau}{d_\infty}s^2 = \frac{\sigma_T s\cos\Theta}{\sqrt{\pi}}\left\{e^{-s^2\sin^2\Theta} + \sqrt{\pi}s\sin\Theta[1+\mathrm{erf}(s\sin\Theta)]\right\} \quad (28)$$

$$\frac{Q\beta^3}{\rho_\infty} = \left(\left[s^2 + \frac{\tilde{\gamma}}{\tilde{\gamma}-1} - \frac{\tilde{\gamma}+1}{2(\tilde{\gamma}-1)}\frac{T_W}{T_\infty}\right]\left\{e^{-s^2\sin^2\Theta} + \sqrt{\pi}s\sin\Theta \times [1+\mathrm{erf}(s\sin\Theta)]\right\} - 0.5e^{-s^2\sin^2\Theta}\right)\left(\frac{a_C}{4\sqrt{\pi}}\right) \quad (29)$$

Equation (29) describes the heat flux of an elemental panel. To calculate the maximum heat transfer for the entire spacecraft, the heat flux of all the individual panels are compared, and the maximum value is selected. Equations (27) and (28) lead to the evaluation of C_p and C_τ as follows[20]:

$$C_p = \Delta p/d_\infty, \qquad C_\tau = \Delta\tau/d_\infty \quad (30)$$

Finally, the aerodynamic forces and moments on the body can be evaluated by summing over the elemental flat panels as follows[20]:

$$\frac{\boldsymbol{F}}{d_\infty A} = \sum_{i=1}^{p}\left\{C_{p_i}(-\hat{\boldsymbol{n}}_i) + C_{\tau_i}[\hat{\boldsymbol{n}}_i \times (\hat{\boldsymbol{V}}\times\hat{\boldsymbol{n}}_i)]\right\} \quad (31)$$

$$\frac{\boldsymbol{M}}{d_\infty Ac} = \sum_{i=1}^{p}\left(\boldsymbol{r}_i \times \left\{C_{pi}(-\hat{\boldsymbol{n}}_i) + C_{\tau_i}[\hat{\boldsymbol{n}}_i \times (\hat{\boldsymbol{V}}\times\hat{\boldsymbol{n}}_i)]\right\}\right) \quad (32)$$

For the flow regime in the continuum domain, Eqs. (27–29) are replaced by the Newtonian approximation such that $s\to\infty$ and $\sigma_T\to 0$. Finally, for the case of transition flow, a logarithmic interpolation with respect to the Knudsen number is employed between the values calculated for the free-molecular flow and the continuum flow regimes. It must be emphasized that there is no attempt to use Eqs. (27–32) for continuum flow modeling as such. The aforementioned Newtonian approximation has been used to have an estimate for continuum flow, which is in turn used as a base to obtain the transition flow properties by interpolation between free-molecular flow and the Newtonian flow.

Results

Spacecraft Model

The atmospheric passes have been simulated using a "box-wing" model for the spacecraft as shown in Fig. 2. The spacecraft without the panels deployed can be approximated by a box $2.2\times 2.6\times 1.7$ m, which is representative of the Odyssey spacecraft.[22] Odyssey can be modeled as having two 2.5-m-long panels at the back of the box, each deployed at 90 deg with respect to the velocity vector.[22] For our simulations, we have modified the configuration of Odyssey by bringing the panels to the front of the spacecraft and increasing their individual lengths to 7.2 m. This has been done to make the spacecraft more amenable to aerocapture. The nominal deployment for either panel is 65 deg, about the pitch axis, as shown in Fig. 2. The spacecraft mass is taken to be 475 kg, and the moments of inertia are $J_{11}=492$, $J_{22}=183$, and $J_{33}=516$ (all in kg · m^2) about the center of mass, which lies at the centroid of the box.

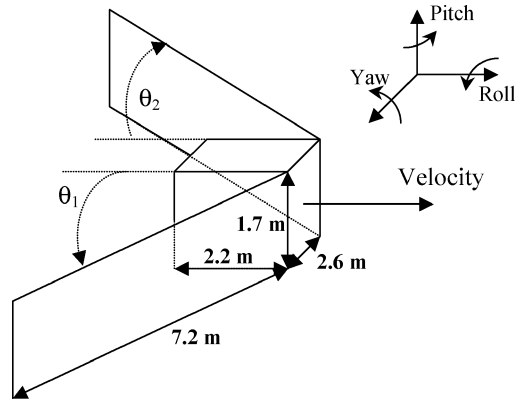

Fig. 2 Spacecraft model.

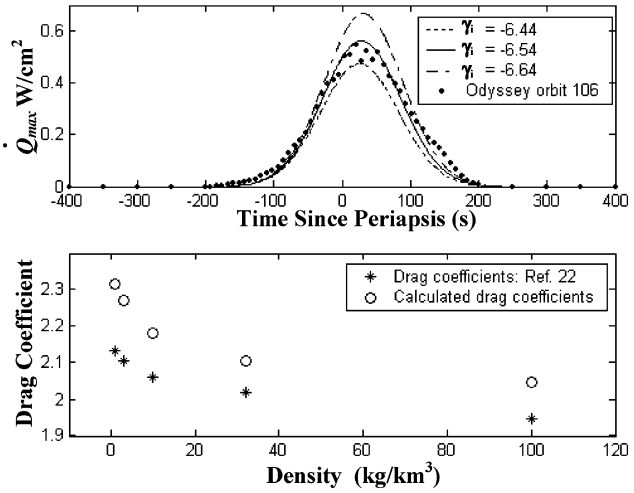

Fig. 3 Heat flux and drag coefficient calculated for Odyssey spacecraft.

Aerothermodynamic Model Validation

Figure 3 shows the maximum heat flux profile and drag coefficients obtained for an aerobraking pass in the Martian atmosphere. For this purpose, panel size and configuration corresponding to the Odyssey spacecraft[22] have been used. The simulations have been carried out for three different initial flight-path angles: −6.44, −6.54, and −6.64 deg. The quaternion components have been adjusted to correspond to zero angle of attack and sideslip at reentry. The Viking density profile[20] has been used in these simulations. The heat flux profile experimentally measured on the 106th orbit (during which the greatest heat flux was recorded) of the Odyssey aerobraking mission[8] has been shown in Fig. 3 for comparison. The difference between calculated drag coefficient values and those reported in Ref. 22 is less than 5.5% for densities greater than 10 kg/km^3, and less than 8.6% for densities smaller than 10 kg/km^3 (Fig. 3). Furthermore, drag coefficients calculated using the aforementioned aerodynamic model have been validated for a cone and a flat plate against analytical results available for such shapes in free-molecular flow.

Earth Aerocapture and Aerobraking

The nominal (noninertial) initial conditions for the first atmospheric pass (i.e., aerocapture) are as follows: $V=12$ km/s; entry altitude = 300 km; $\gamma=-11.72$ deg; $\chi=29.8$ deg; $\delta=-132$ deg; and $\gamma=-23$ deg. The quaternion components are adjusted to give zero angle of attack at the start of atmospheric entry. The nominal flight-path angle has been obtained by trial and error and corresponds to a shallow entry trajectory.

Table 1 shows the relevant results of atmospheric passes 1 through 6. The nominal initial flight-path inclination of −11.72 deg for aerocapture gives a moderate heat flux and a convenient final orbit with a 10.5-h period (which allows sufficient time for orbit determination and correction) and a sufficiently low eccentricity (0.734). During the aerobraking phase, the peak heat flux is substantially smaller compared to that for aerocapture. Passes 3–5 achieve essentially the same velocity decrement, because their zone of operation is about the same (low points of 100–102 km). It can be seen in Table 1 that, although the velocity change remains approximately the same in these passes, the peak heat flux reduces steadily. This is due to the fact that the time spent inside the atmosphere increases with each pass. Consequently, the drag force accumulated over time remains approximately the same for these passes, although the peak heat flux decreases due to lower velocities in successive passes. The time spent inside the atmosphere is reflected in the heat load: the

Table 1 Results at the end of each atmospheric pass

Pass	V_i^*, m/s	γ_i^*, deg	ΔV, m/s	$\dot{Q}_{\max}$, W/cm^2	Q, Ws/cm^2 ($\times 10^{-4}$)	Final eccentricity, e	Period, h	Low point, km	ΔV at apoapse, m/s	New low point, km
					$\Sigma = 21.65$				$\Sigma = 66.46$	
1	12383	−11.35	2234	450	11.76	0.734	10.5	86.6	0.48	90
2	10148	−9.38	1341	149	5.83	0.322	2.57	88.5	2.73	100
3	8809.4	−6.87	302.7	20.6	1.15	0.235	2.16	99.2	0.20	100
4	8504.3	−6.03	352.1	18.9	1.29	0.140	1.81	98.4	1.00	102
5	8150.9	−4.70	369.4	13.0	1.28	0.044	1.54	96.4	5.49	115
6	7786.4	−2.41	106.0	1.7	0.34	0.017	1.48	108	56.6	300

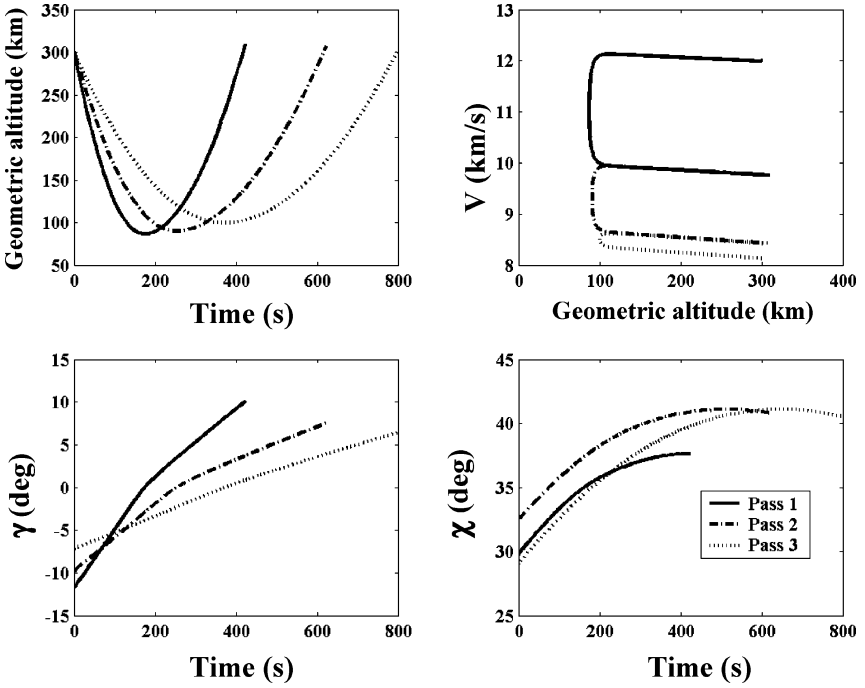

Fig. 4 Important trajectory parameters during passes 1–3.

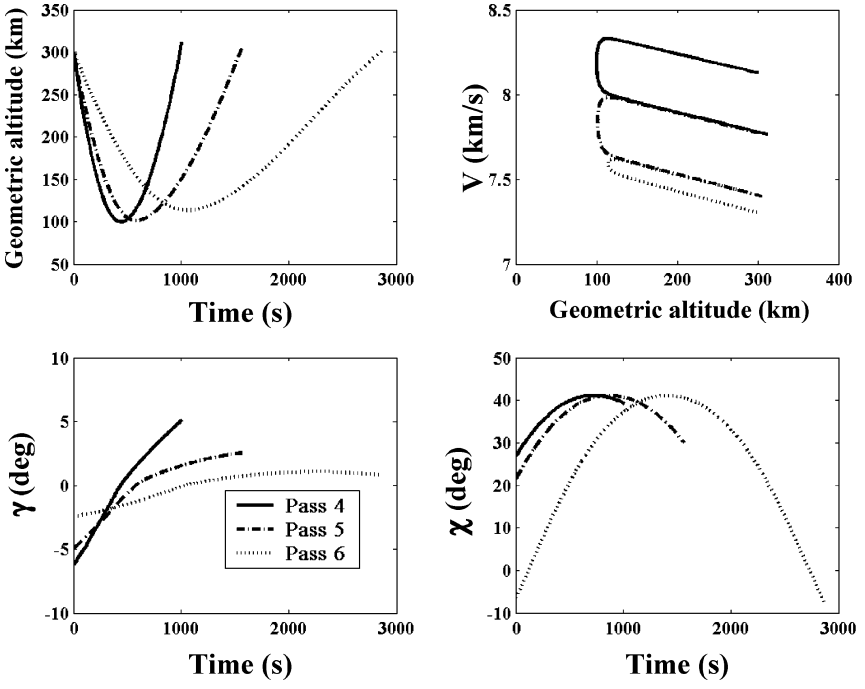

Fig. 5 Important trajectory parameters during passes 4–6.

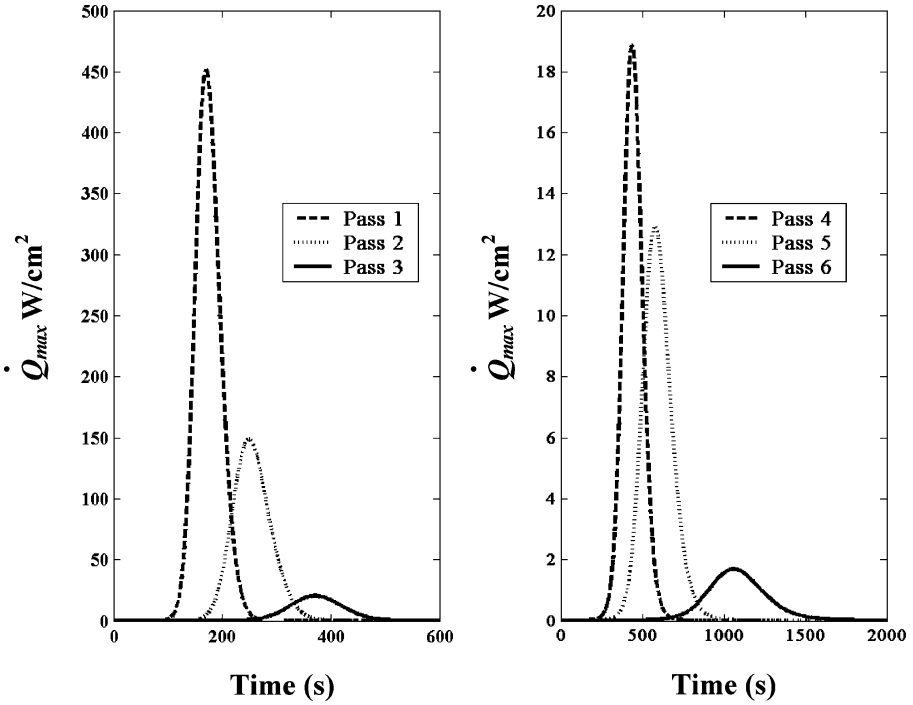

Fig. 6 Peak convective heat flux during the braking mission.

total heat transfer by convection during a pass, which remains approximately the same for passes 3–5. At the end of the sixth pass, the apoapsis of the orbit is 330 km, and an apoapsis burn of 56.6 m/s is required to raise the periapsis to 300 km, resulting in a practically circular orbit ($e = 0.0022$). Hence, the circular orbit is accomplished within 20 h of the first entry with a total impulse of 66.46 m/s, which is only 6.7 kg of propellant for an initial mass of 475 kg, assuming a specific impulse of 480 s. This is less than 1.5% of the spacecraft mass. In comparison, only the MOI required about 35% of the Odyssey spacecraft mass. The elliptical to circular aerobraking results may also be contrasted with those reported by French and Cruz[3] for Earth, where a ΔV requirement of 142 m/s (excluding the capture burn) has been stated, with the braking mission spanning 10 days for achieving a 300-km final circular orbit, starting with a 12-h elliptic orbit.

Figures 4 and 5 show the trajectories for all the passes, and Fig. 6 shows the observed peak convective heat fluxes. The angle of attack and sideslip are seen to be close to zero (within ± 2 deg) during the first and all the subsequent passes. The body attitude is seen to oscillate with a frequency of 3.1 rad/s below 150 km altitude. Figure 7, for the first pass, is typical. Figure 8 shows the inertial flight-path-angle evolution over the entire braking mission. It is clear from this figure that at the end of the mission, with the final apoapsis burn, a near-circular orbit is established. It was observed that despite the hyperbolic speed of the spacecraft during the aerocapture, the drag experienced by it at altitudes above 120 km is not significant to cause a noticeable change in speed. Most of the speed decrement (Figs. 4 and 5) is obtained in the altitude range from 105 to 86 km.

Table 2 Effect of initial flight-path angle on the first atmospheric pass

γ_i, deg	Low point, km	Maximum density, kg/m^3 ($\times 10^6$)	ΔV, m/s	$\dot{Q}_{\max}$, W/cm^2	Aerocapture successful? (e, period)
−11.60	91.08	2.853	1039	229	No (1.151)
−11.65	89.20	3.998	1418	305	No (1.014)
−11.66	88.84	4.268	1511	323	Yes (0.981, 551.0 h)
−11.67	88.47	4.565	1611	342	Yes (0.946, 114.7 h)
−11.68	88.10	4.884	1718	362	Yes (0.909, 52.23 h)
−11.70	87.34	5.615	1957	405	Yes (0.827, 20.01 h)
−11.71	87.00	5.978	2091	428	Yes (0.782, 14.14 h)
−11.72	86.57	6.473	2234	450	Yes (0.734, 10.48 h)
−11.73	86.17	6.972	2393	477	Yes (0.683, 8.06 h)
−11.74	85.80	7.443	2561	503	Yes (0.629, 6.36 h)
−11.75	85.40	7.955	2740	527	Yes (0.573, 5.14 h)
−11.80	83.40	11.049	3922	654	Yes (0.223, 2.09 h)
−11.82	82.50	12.674	4631	709	Yes (0.037, 1.50 h)
−11.83	0	Strikes the planet surface			No

Sensitivity Analysis

The six-DOF dynamic model permits an analysis of the stability of the spacecraft motion due to perturbation in various parameters. Here we present the sensitivity of the spacecraft motion with respect to the initial flight-path angle, differential panel deployment, initial angle of attack, and initial body rates.

Sensitivity to Initial Flight-Path Angle

For the first atmospheric pass (aerocapture maneuver), the results of variation in initial relative flight-path angle are shown in Table 2. It is evident that the flight-path angle is a very sensitive mission variable. This is because although a slight change in γ causes a minor change in the low point of the trajectory, the density increases significantly, which causes a significant rise in the velocity decrement. The ratio of velocity decrement is in step with the ratio of densities. For the case of $\gamma_i = -11.66$ deg, the spacecraft is only just captured by the planet and enters a highly eccentric orbit of 551-h period. Nevertheless, it is not lost and can still be established in a circular orbit using six passes, with peak heat transfer rates of 323, 166, and 136 W/cm^2 for the first, second, and third passes, respectively (compared to 450, 149, and 20.6 W/cm^2 for the nominal mission). At the end of the third pass with these increased peak heat

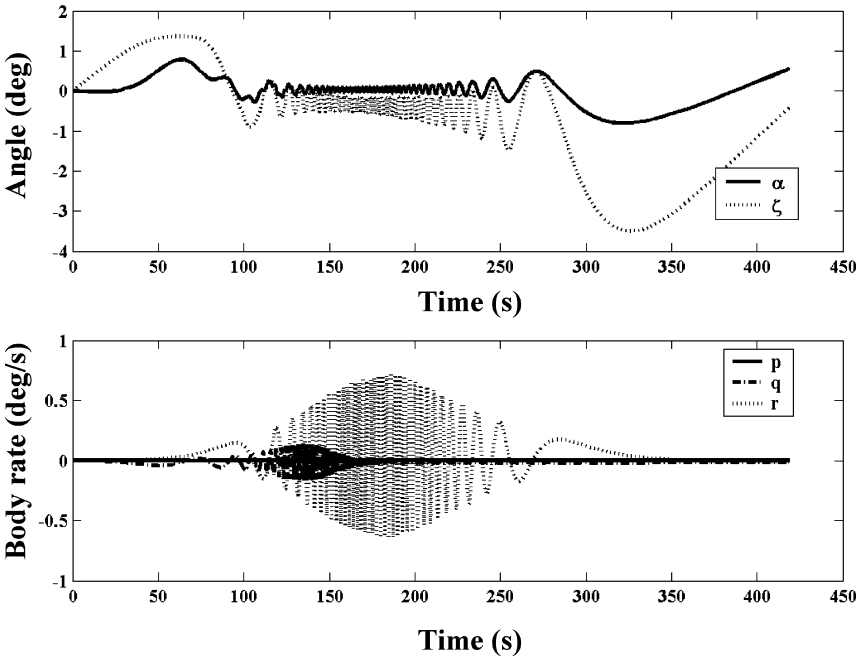

Fig. 7 Flow angles and angular motion during the first pass.

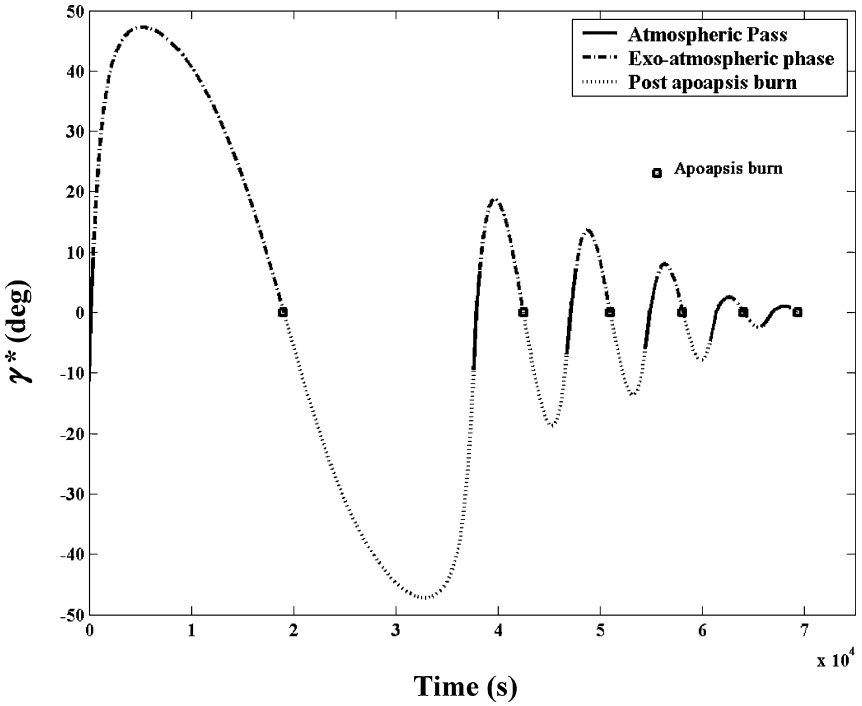

Fig. 8 Evolution of the inertial flight-path angle over the entire braking mission.

transfer rates, the orbit is reduced to an eccentricity of 0.16 and is in approximately in the same state as it was at the end of the third pass for the nominal mission. On the other extreme, $\gamma_i = -11.82$ deg is the upper limit for the initial relative flight-path angle because, beyond this value, the spacecraft experiences too much drag and hits the Earth's surface.

Sensitivity to Panel Deployment

The static stability of the spacecraft shown in Fig. 2 depends strongly on the angles by which the panels are deployed. It can be easily seen from Fig. 2 that the maximum permissible deployment angle of both panels is 72 deg, beyond which the spacecraft becomes statically unstable because the center of pressure of the panels moves forward of the center of gravity. This is indeed observed to be the case upon running simulations for such deployment angles.

There might be a situation in which the panels are deployed asymmetrically. Such off-design panel deployment occurred during the aerobraking of the MGS,[23] which led to a complete reworking of its aerobraking strategy. For the configuration presented in this paper, the effect of differential panel deployment on the trajectory was studied. Table 3 and Fig. 9 contain the results for the first pass. It is observed that as θ_2 is increased above the nominal deflection, while keeping θ_1 at nominal, the spacecraft has a tendency toward

Table 3 Effect of panel deployment error on trajectory parameters

θ_1, deg	θ_2, deg	ζ_{mean}, deg	α_{mean}, deg	Frequency, rad/s	$\dot{Q}_{\max}$, W/cm^2	ΔV, m/s	Peak normal load, g	Peak axial load, g	Aerocapture successful? (e_f, period)
65	65	−0.4	0	3.14	450	2234	0.011	3.88	Yes (0.734, 10.5 h)
65	75	−0.5	−9.1	7.54	438	2402	0.310	4.23	Yes (0.679, 7.90 h)
65	70	−0.4	−4.2	8.48	446	2335	0.130	4.15	Yes (0.701, 17.99 h)
65	60	−0.5	−13.8	9.74	455	1996	0.084	3.80	Yes (0.817, 18.41 h)
65	45	−1.0	13.7	10.68	457	1720	0.186	3.15	Yes (0.901, 52.42 h)
65	40	−1.3	16.8	11.31	456	1584	0.188	2.91	Yes (0.956, 155.88 h)
65	35	−1.5	19.7	11.94	454	1451	0.180	2.68	No (1.003)
65	25	2.4	25.5	11.94	446	1193	0.150	2.21	No (1.095)
65	0	−6.0	39.4	11.94	408	644	0.059	1.15	No (1.299)

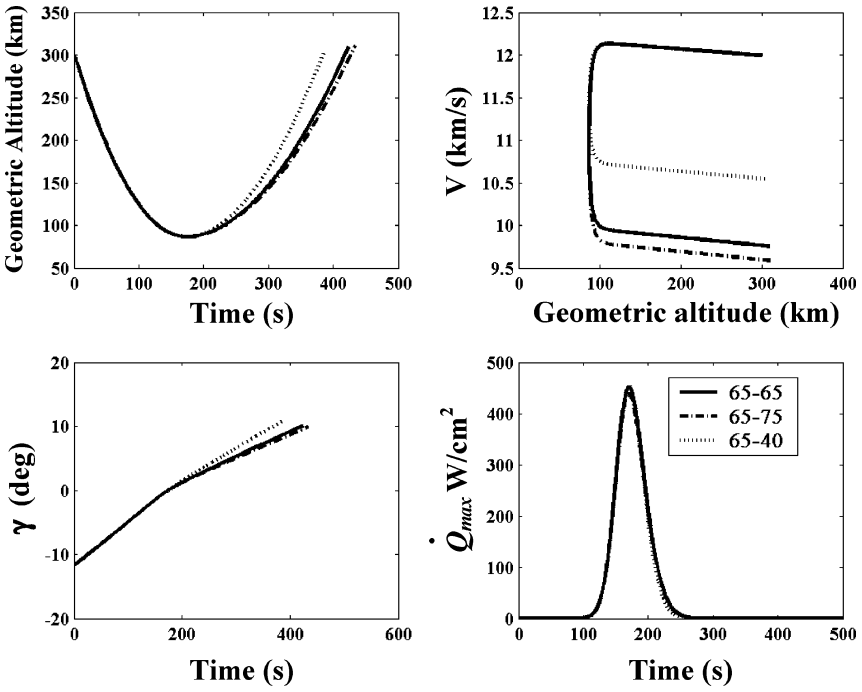

Fig. 9 Trajectory for the first pass with differential deflection of panels.

instability. This is to be expected from the observations made earlier about its static stability. At a deployment of 80 deg, the vehicle becomes unstable, and the angle of attack grows large. However, once the angle of attack increases beyond 100 deg, the aerodynamic model used in this study becomes invalid for force/moment prediction for the stated deployment angle of 80 deg. This is because, at an angle of attack greater than 100 deg, the spacecraft with one panel deployed at 80 deg will experience flow from the "back," in which case the body seeing the flow is no longer convex. Therefore, the collisionless nature of the reflected flow is not maintained, and the aerodynamic calculations will be erroneous. However, it can be stated that, for the case of panel deployment of 80 deg and above for one panel (with the other at nominal), the angle of attack grows large while the spacecraft is inside the atmosphere, which is undesirable.

On the other hand, a deployment of less than nominal is more tolerable in terms of stability but causes a smaller speed decrement in the pass. Indeed, it is expected that the error in deployment of the actual spacecraft would be on the lesser side of nominal rather than on the higher side. Therefore, as is evident from Table 3, stability would not be a problem for the mission. However, a deployment error of −25 deg on one panel (65, 40 deg) causes the drag to be significantly low. Indeed, the spacecraft is barely captured in this case, and the resulting orbit is not at all desirable (156-h period). Furthermore, the peak frequency of motion is greater than 10 rad/s for the (65, 45 deg) case and all cases with less than 45-deg deployment. This is not desirable from the structural point of view. Therefore, the proper deployment of the panels is a crucial factor during aerocapture.

Hence, it emerges from the preceding analysis that the spacecraft configuration used allows for significant differential deflection of the panels without causing stability problems, although an error in panel deployment of 25 deg on the lower side will lead to unsuccessful aerocapture.

Sensitivity to Initial Angle of Attack, Sideslip, and Body Rates

For the atmospheric passes shown in Tables 1 and 3, the angle of attack and sideslip at the start of entry has been taken to be zero. However, the anomalous functioning of the onboard attitude control system may cause a large initial nonzero flow angles.

It is observed that the spacecraft seeks out a zero angle of attack and sideslip despite starting from a perturbed value as high as 100 deg (Table 4 and Fig. 10). The fact that the entry is begun at

Table 4 Effect of initial angle of attack and sideslip on trajectory parameters

α_I, deg	ζ_I, deg	α (Peak amplitude), deg	ζ (Peak amplitude), deg	Oscillation frequency, rad/s	Peak normal load, g	Peak axial load, g	$\dot{Q}_{\max}$, W/cm^2	ΔV, m/s
0	0.0	0.14	0.5	3.14	0.011	3.88	450	2234
−20	−4.8	2.0	1.1	6.28	0.081	3.88	451.5	2234
−40	−7.5	5.0	2.0	6.28	0.152	3.88	451.5	2233
−60	0.0	7.0	2.5	6.60	0.24	3.88	451.5	2228
−100	−3.5	16.1	3.2	6.60	0.55	3.89	453	2190
−100	−40	16.1	13.2	6.91	0.55	3.89	453	2189

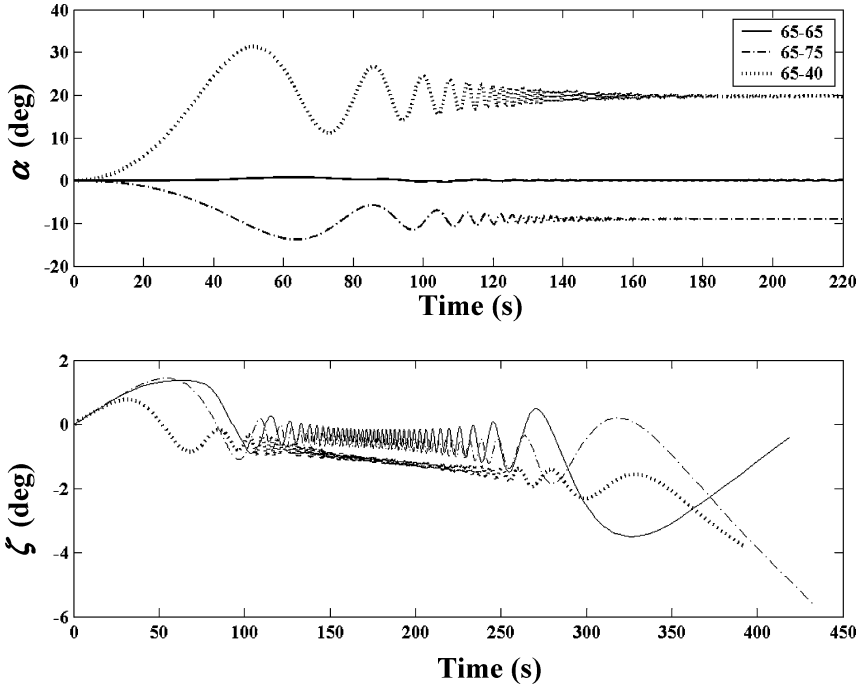

Fig. 10 Flow angles with differential panel deflection for the first pass.

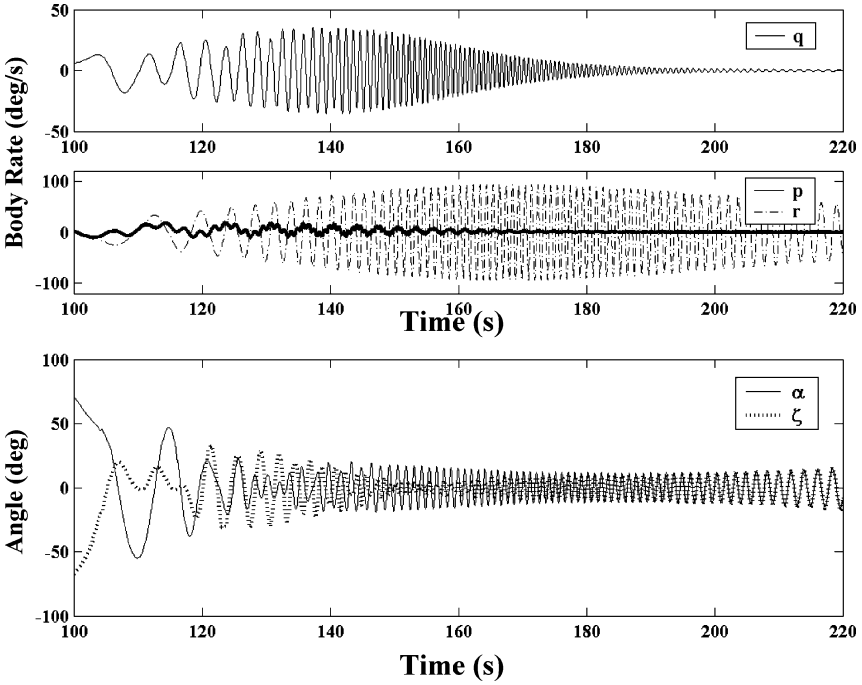

Fig. 11 Attitude sensitivity to initial yaw, pitch, and roll rates of 0.1 rad/s.

300 km gives the spacecraft sufficient time to orient itself to a zero mean angle of attack before it experiences sizeable disturbing moments from the atmosphere. The oscillation frequency below 120 km is around 6.2 rad/s and will require structural reinforcement of the panel. This is the case for all the passes. The peak amplitudes observed below 120 km altitude are tabulated in Table 4. Furthermore, the trajectory parameters remain almost the same as for the nominal conditions because of the fact that the spacecraft has a zero mean angle of attack while inside the dense atmosphere. Consequently, no noticeable departures from nominal values of velocity decrement, exit flight-path angle, or the maximum convective heat flux are observed (Table 4).

Initial body rates of 0.1 rad/s about all three principle axes cause the angle of attack and sideslip to grow initially. However, as is visible in Fig. 11, they oscillate with smaller amplitude once inside the dense atmosphere, and the resulting motion is stable.

Conclusions

A combination of the aerocapture and aerobraking maneuvers has been shown to achieve a circular orbit ($e = 0.017$) from an open orbit of high initial eccentricity ($e = 1.55$). The braking mission is accomplished in a short span (20 h) and with meager propellant expenditure. The heat flux during the maneuver is well within the capability of the PICA, which will have to be used on the spacecraft shown. However, coating of PICA on the panels will certainly complicate their use as solar arrays (the leeward faces could be used as solar arrays, while the windward surfaces constitute a heat shield), and a careful design is required for stowage and deployment of the panels. Furthermore, the structural design of the panels should consider the aerothermoelastic loads encountered in each pass. If such design issues are resolved, the strategy, applied to an Earth capture of a space tug or a planetary mapping mission, will lead to enormous savings of fuel. As expected, the initial flight-path angle for aerocapture is an extremely sensitive parameter and needs to be maintained precisely by active exoatmospheric guidance. The sensitivity analysis has revealed a high degree of atmospheric flight stability of the spacecraft despite large perturbations in initial angle of attack, sideslip, body rates, and differential panel deployment, primarily due to the large swept-back panels. This implies that there is no requirement for an active attitude control of the spacecraft during the atmospheric phase, even if the reentry attitude and spin are anomalous.

References

[1]Walberg, G. D., "A Survey of Aeroassisted Orbit Transfer," *Journal of Spacecraft and Rockets*, Vol. 22, No. 1, 1985, pp. 3–18.

[2]Parkinson, B., "Planetary Exploration—Towards New Worlds or New Possibilities," *Journal of the British Interplanetary Society*, Vol. 54, Aug. 2001, pp. 229–235.

[3]French, J. R., and Cruz, M. I., "Aerobraking and Aerocapture for Planetary Missions," *Aeronautics and Astronautics*, Vol. 18, No. 2, 1980, pp. 48–55, 71.

[4]Repic, E. M., Boobar, M. G., and Chapel, F. G., "Aerobraking as a Potential Planetary Capture Mode," *Journal of Spacecraft and Rockets*, Vol. 5, No. 8, 1968, pp. 921–926.

[5]Lyons, D. T., Sjogren, W., Johnson, W. T. K., Schmitt, D., and McRonald, A., "Aerobraking Magellan," American Astronautical Society, Paper 91-420, Aug. 1991.

[6]Johnston, M. D., Esposito, P. B., Alwar, V., Demcak, S. W., Graat, E. J., and Mase, R. A., "Mars Global Surveyor Aerobraking at Mars," American Astronautical Society, Paper 98-112, Feb. 1998.

[7]Lyons, D. T., Beerer, J. G., Esposito, P., Johnston, M. D., and Wilcockson, W. H., "Mars Global Surveyor: Aerobraking Mission Overview," *Journal of Spacecraft and Rockets*, Vol. 36, No. 3, 1999, pp. 307–313.

[8]Hanna, J. L., Tolson, R., Cianciolo, A. D., and Dec, J., "Autonomous Aerobraking at Mars," 5th International ESA Conf. on Guidance Navigation and Control Systems and Actuator and Sensor Product Exhibition, Oct. 2002.

[9]Miele, A., Wang, T., Lee, W. Y., and Zhao, Z. G., "Optimal Trajectories for the Aeroassisted Flight Experiment," *Acta Astronautica*, Vol. 21, Nos. 11/12, 1990, pp. 735–747.

[10]Gurley, J. G., "Guidance for an Aerocapture Maneuver," *Journal of Guidance, Control, and Dynamics*, Vol. 16, No. 3, 1993, pp. 505–510.

[11]Evans, S. W., and Dukeman, G. A., "Examination of a Practical Aerobraking Guidance Algorithm," *Journal of Guidance, Control, and Dynamics*, Vol. 18, No. 3, 1995, pp. 471–485.

[12]Miele, A., and Wang, T., "Robust Predictor-Corrector Guidance for Aeroassited Orbital Transfer," *Journal of Guidance, Control, and Dynamics*, Vol. 19, No. 7, 1996, pp. 1134–1141.

[13]Powell, R. W., and Braun, R. D., "Six-Degree-of-Freedom Guidance and Control Analysis of Mars Aerocapture," *Journal of Guidance, Control, and Dynamics*, Vol. 16, No. 6, 1993, pp. 1038–1044.

[14]Johnson, W. R., Longuski, J. M., and Lyons, D. T., "Attitude Control During Autonomous Aerobraking for Near-Term Mars Exploration," American Astronautical Society, Paper 01-388, July–Aug. 2001.

[15]Puig-Suari, J., Longuski, J. M., and Tragesser, S. G., "Aerocapture with a Flexible Tether," *Journal of Guidance, Control, and Dynamics*, Vol. 18, No. 6, 1995, pp. 1305–1312.

[16]Lohar, F. A., Misra, A. K., and Mateescu, D., "Optimal Atmospheric Trajectory for Aerogravity Assist with Heat Constraint," *Journal of Guidance, Control, and Dynamics*, Vol. 18, No. 4, 1995, pp. 723–730.

[17]Tran, H., Johnson, C., Rasky, D., Hui, F., Chen, Y. K., and Hsu, M., "Phenolic Impregnated Carbon Ablators (PICA) for Discovery Class Missions," AIAA Paper 96-1911, June 1996.

[18]Desai, P. N., Mictheltree, R. A., and Cheatwood, F. M., "Entry Dispersion Analysis for the Stardust Comet Sample Return Capsule," AIAA Paper 97-3812, Aug. 1997.

[19]Vinh, N. X., "Equations of Motion," *Flight Mechanics of High Performance Aircraft*, Cambridge Aerospace Series 4, Cambridge Univ. Press, New York, 1993.

[20]Regan, F. J., and Anandakrishnan, S. M., "Flowfield Description," *Dynamics of Atmospheric Re-Entry*, 1st ed., edited by J. S. Przemieniecki, AIAA Education Series, AIAA, Washington, DC, 1993, pp. 318–321.

[21]Bird, G. A., "Collisionless Flows," *Molecular Gas Dynamics*, Clarendon, Oxford, 1976.

[22]Chavis, Z. Q., and Wilmoth, R. G., "Plume Modeling and Application to Mars 2001 Odyssey Aerobraking," AIAA Paper 2002-2896, June 2002.

[23]Lyons, D. T., "Mars Global Surveyor: Aerobraking with a Broken Wing," American Astronautical Society, Paper 97-618, Aug. 1997.

C. McLaughlin
Associate Editor